ACS Energy LETTERS

http://pubs.acs.org/journal/aelccp

Iodine and Sulfur Vacancy Cooperation Promotes Ultrafast Charge Extraction at $MAPbI_3/MoS_2$ Interface

Yongliang Shi, Oleg V. Prezhdo, Jin Zhao,* and Wissam A. Saidi*

Cite This: *ACS Energy Lett.* 2020, 5, 1346−1354

Read Online

ACCESS | Metrics & More | Article Recommendations | Supporting Information

ABSTRACT: It is crucial to optimize hole transport materials (HTMs) to improve the performance of metal halide perovskites solar cells. While atomically thin two-dimensional transition metal chalcogenides (TMDs) are promising HTM candidates because of their high charge mobility, the nature of the formed type I heterojunction hampers the transfer of photoexcited holes. We show that a small concentration of sulfur vacancies (S_V) is already sufficient to stabilize iodine vacancies (I_V) at the $MAPbI_3/MoS_2$ interface (S_V-to-I_V process), to induce an interface dipole moment, and to reverse the offset of the valence band maxima, thus leading to ultrafast hole transport from the absorber to the electrode. The 0.2−0.8 ps time scale computed from nonadiabatic density functional theory is in agreement with experiment. Our results prove that the "S_V-to-I_V" interface vacancy engineering plays the crucial role in improving the HTM performance of TMDs.

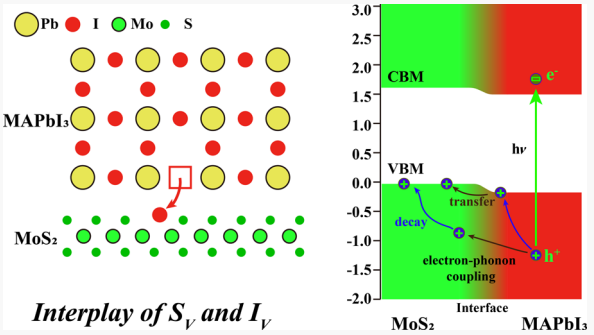

Metal halide perovskites (MHPs), and in particular, $MAPbI_3$ (MA = CH_3NH_3) have generated a lot of interest in the field of photovoltaics.[1−3] In the past decade, significant efforts have been made from material growth to device fabrication, resulting in substantial improvements in the record cell efficiency of perovskite solar cells (PSCs) from 3.8% to 25.2%,[4] surpassing many conventional semiconductor absorbers. These advancements are due to the unique characteristics of $MAPbI_3$, including large absorption coefficient >3.0 × 10^4 cm^{-1} in the visible light region,[5] low exciton binding energy resulting in high quantum yield of free electrons and holes,[6] long electron−hole diffusion lengths,[7−10] and electronically benign point[11,12] and grain-boundary defects.[13] Although MHP absorbers are relatively cheap, the PSCs are still not cost-effective because of the expensive hole transport material (HTM) that is used to shuttle the generated holes from the absorber to the electrode.[14] The HTM in state-of-the-art PSCs is an organic polymer called spiro-OMeTAD,[15] which currently has a commercial price of $312/g, which is ∼8 times more expensive than gold ($43/g).[16] Further, recent studies have also linked the long-term operational and thermal instability of the PSCs to the organic spiro-OMeTAD polymer or its ingredients.[17,18] While there have been many materials that are proposed and tested as HTMs,[19,20] spiro-OMeTAD still represents to date the reference HTM.[21] This underscores the complexity of finding new candidate materials and also of their optimization.

As coined by Kroemer,[22] "the interface is the device." In PSCs, it is generally believed that the major limiting factor of charge carrier transport is due to the contact layers rather than the perovskite absorber.[23−25] Finding a successful contact material is challenging as it has to satisfy several requirements in terms of its chemical, optical, and electric properties.[15,26,27] For PSCs, the valence band (VB) energy of the HTM has to be higher than that of the absorber so that it can trap the photoexcited holes efficiently. In addition, for facile charge-transfer requirements, the charge transport layers have to satisfy other requirements, including chemical stability and hydrophobicity to enhance resilience of the solar cell in humid environments.

Atomically thin two-dimensional TMDs are promising HTM candidates because of their high mobility. Unfortunately, the work functions (WFs) of pristine TMDs are higher than MHPs by ∼0.8 eV,[28] which hampers the transfer of

Received: March 1, 2020
Accepted: March 30, 2020
Published: March 30, 2020

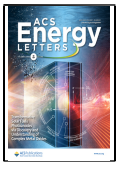

https://dx.doi.org/10.1021/acsenergylett.0c00485
ACS Energy Lett. 2020, 5, 1346−1354

photoexcited holes. Peng and collaborators[28] have shown that the creation of S_V of varying concentrations through a mild O_2 plasma treatment results in ultrafast hole transfer within 300−700 fs between MHP and vacancy-engineered MoS_2, suggesting that vacancy engineering in TMDs may play an important role in making them promising HTMs. However, the atomic mechanism of such vacancy engineering is not clear. First, past research suggested that the band edges of MoS_2 can be tuned by dopant type and doping concentration.[29,30] However, the change of band edges is generally not large enough to reverse the band offset between MoS_2 and $MAPbI_3$.[30−32] Others proposed the electron injection mechanism in which S_V can induce band gap states that can be used for hole trapping.[28,33−37] However, to generate n-type band gap states, the ratio of S and Mo needs to be as small as 1.8:1,[38] suggesting the S_V concentration needs to be as high as 20%. By contrast, in real experiments, the concentration of S_V is generally less than 4.4%.[38−43] Further, the generation of vacancies and dopings in TMDs should affect the interface structure significantly, yet this is excluded in previous investigations.

In this Letter, taking $MAPbI_3/MoS_2$ as a prototypical system, we study in detail how the vacancy engineering affects the interface properties and the excited hole transport dynamics at the TMD/perovskite interface. We propose a new mechanism for changing TMDs into efficient HTM through vacancy engineering based on *ab initio* molecular dynamics (AIMD) and nonadiabatic molecular dynamics (NAMD) simulation. We show that although pristine MoS_2 is not a viable HTM layer, only a low concentration of S_V can improve its performance significantly through an interfacial interaction with $MAPbI_3$. This is because S_V can easily promote the formation of iodine vacancies[44] (I_V) at the interface, and such a "S_V-to-I_V" chain generation of vacancies will induce interfacial dipole moment and reverse the band offset between MoS_2 and $MAPbI_3$. Further, NAMD simulations show that the hole transfer to MoS_2 will take place within several hundreds femtoseconds, which is faster than the electron−hole recombination at vacancies by 3 orders of magnitude, further supporting its excellent performance as HTM layer. Our results prove that the "S_V-to-I_V" vacancy engineering mechanism plays the key role in making MoS_2 a promising HTM. We propose that the conclusion can be extended into other TMD systems, providing new insights into the functional HTM design.

The AIMD simulations and electronic structure calculations are performed using the Vienna ab initio simulation package (VASP).[45−47] The NAMD simulations are performed by Hefei-NAMD,[48] which augments VASP with the NAMD capabilities similar to ref 49. This approach has been successfully applied to photocatalysis,[50] electron−hole recombination,[51−58] and van der Waals heterostructure interface.[59,60] The electron−nuclei interactions are described using the projector augmented wave method[61] and the Perdew−Burke−Ernzerhof exchange−correlation functional are used.[62] The electronic wave function is expanded using plane waves with an energy cutoff of 400 eV. The K-point mesh uses Γ point only justified by the employed large supercell. After geometry optimization, we use velocity rescaling to bring the system's temperature to 300 K. A 5 ps microcanonical AIMD trajectory is then generated with a time step of 1 fs. We use Kohn−Sham (KS) orbitals of configurations from the AIMD trajectory to compute the nonadiabatic coupling (NAC) and then carry out the NAMD simulations. The NAMD results are based on an average over 100 different initial configurations obtained from the AIMD trajectory. For each chosen initial configuration, we sample 2×10^4 trajectories. The trajectories are reused to achieve sufficient simulation time.

To get a preliminary understanding of the band alignment between MoS_2 and $MAPbI_3$, we first investigate their WFs in isolation. Monolayer MoS_2 has a confinement-induced direct bandgap of 1.9 eV at K point in 2D-reciprocal space.[63] Our density functional theory (DFT) calculations confirm a direct bandgap of 1.71 eV that underestimates the experimental value because of the well-known self-interaction error of DFT. The WF of intrinsic monolayer MoS_2 is 5.91 eV as calculated from the difference between VBM and local vacuum, which is close to the experimental (5.90 eV[64]) and previous first-principles (5.86 eV[65]) values.

To determine the WF for $MAPbI_3$, we build a slab with (001) orientation formed from the stacking of PbI_2 and MAI layers, as shown in Figure S2. Although the (001) termination of $MAPbI_3$ is nonpolar because of the zero nominal charges of PbI_2 and MAI layers, MA is a polar molecule (dipole 2.73 D[66]), and thus, different arrangements of the MA molecule, facilitated by the relatively small rotation barrier,[67] are expected to yield different WFs of the slab. To study the impact of the MA dipole on the $MAPbI_3/MoS_2$ heterostructure, we investigate four different configurations that differ in the initial orientation of the MA dipoles. In the "MA-half" configuration, the molecular dipoles in adjacent layers are inverted with respect to each other (Figure S2a), while as in the "MA-down" and "MA-up" slabs, all MA molecules are oriented in one direction either toward or away from the PbI_2 layer. On the other hand, for the "MA-parallel" case, all MA molecules are parallel to the surface to minimize the MA-dipole perpendicular to the slab. After structural optimization, the WF values are found to vary between 4.35−5.49 eV. As seen from Figure S2, at the PbI_2 interface, the WF is around ∼5.4 eV and varies by only ∼0.1 eV depending on the polarity of the slab, while as for the "polar" MAI interface the WF shows more variations. Nevertheless, and regardless of the termination and the polarization of the slab, the heterostructure has a negative band offset as the WF of MoS_2 is ∼0.5 eV larger than that of $MAPbI_3$, and thus, the hole transfer is thermodynamically hindered.

However, our conclusion on the nonfavorable band offset between MoS_2 and $MAPbI_3$ for hole transport cannot be judged from the innate WFs of the individual constituent materials.[68] This is because, in the isolated limit, there is charge relaxation into vacuum that is not present in the "realistic" heterostructure, and it does not account for the interfacial charge transfer that necessarily exists in a realistic interface model. To account for such effects, we construct a $MAPbI_3/MoS_2$ heterostructure model using a large supercell corresponding to $MAPbI_3(\sqrt{2} \times \sqrt{13})/MoS_2(\sqrt{13} \times \sqrt{49})$ that has less than 3% lattice mismatch (see Figure 1). Investigating three different arrangements of the MA dipoles (see Supplementary Note 2), we find after structural optimization that the favorable configuration corresponds to the case with MA dipole moments pointing toward MoS_2 (see Figure S3d−f). Using this structure, we find that the band offset between $MAPbI_3$ and MoS_2 in the realistic model is 0.2 eV that is appreciably smaller than 0.5 eV for the non-interacting system. However, the smaller value does not change our conclusion that pristine MoS_2 is not a suitable a hole

https://dx.doi.org/10.1021/acsenergylett.0c00485
ACS Energy Lett. 2020, 5, 1346−1354

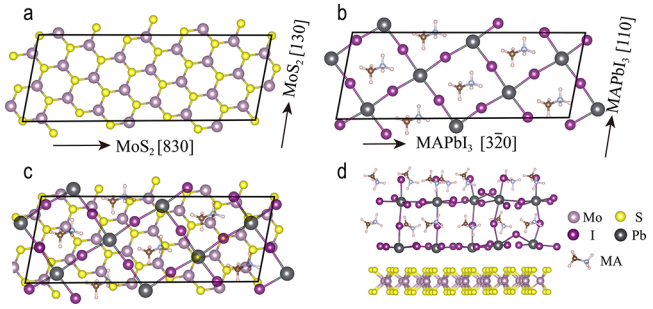

Figure 1. Lattice matched structures of (a) pristine $MoS_2(\sqrt{13} \times \sqrt{49})$ and (b) $MAPbI_3(\sqrt{2} \times \sqrt{13})$ surface slabs along (001) orientation. (c) Top and side views of interface model for $MAPbI_3/MoS_2$ heterostructure.

transport layer for $MAPbI_3$, in agreement with experimental results. Also, temperature renormalization effects of the electronic levels due to electron−phonon coupling are not expected to change this conclusion given their relatively small effect.[69−71]

p-doping of MoS_2 decreases the WF and thus could facilitate hole transport from $MAPbI_3$ to MoS_2, as shown recently via S_V doping.[28] Before investigating how S_V influences the band alignment in the real interface, we consider the isolated MoS_2 layer to gain more insight. Different S_V concentrations up to 25% are generated, including configurations with dispersed or agglomerated defects, as shown in Figure S4. Table S2 shows as expected that the higher the S_V concentration, the lower the WF of MoS_2. For the realistic interface model, we also obtain similar trends, although the changes in the WF with S_V concentration are significantly smaller. For example, the WF decreases by only ∼0.1 eV as S_V increases to 14.4%, while the decrease based on the isolated MoS_2 layer is ∼0.2−0.6 eV. These differences are due to the structural arrangements and screening effects with defected MoS_2 that result in a stronger bonding with $MAPbI_3$ compared to the pristine MoS_2. Our results suggest that an unrealistic relatively large S_V concentration of at least 20% is required to open a hole-transport channel by reversing the band offset of VBM, whereas the reported defect densities range between 0.004% and 4.4%.[38−43] Therefore, we propose that there is a new mechanism besides simple S_V doping that can reverse the band offset.

Because of the attractive interaction between the positively charged S_V and iodine anion, we examined other potential mechanisms to lower band offset based on the interplay between S_V and defect chemistry of $MAPbI_3$. By carefully inspecting an AIMD trajectory obtained at room temperature, we discovered that interfacial iodine could diffuse across the $MAPbI_3/MoS_2$ interface to occupy the S_V site and thus create iodine vacancy (I_V) at $MAPbI_3$ interface. We refer to this configuration as I-filled-S_{nV} with n as the number of S_V that is initially created in MoS_2 and such a chain vacancy generation process as S_V-to-I_V. At T = 0 K we find that it costs only ∼0.2 eV to create I-filled-S_V, while this substitution is favorable by 0.27−0.43 eV for the two higher vacancy concentrations. For the S_{3V} case, we find two different configurations that were particularly stable where the three vacancy locations are located at the vertices of an equilateral triangle with a side equivalent to one and two nearest S−S neighbors (see Figure S4). We refer to these configurations as $S_{3V(1)}$ and $S_{3V(2)}$,

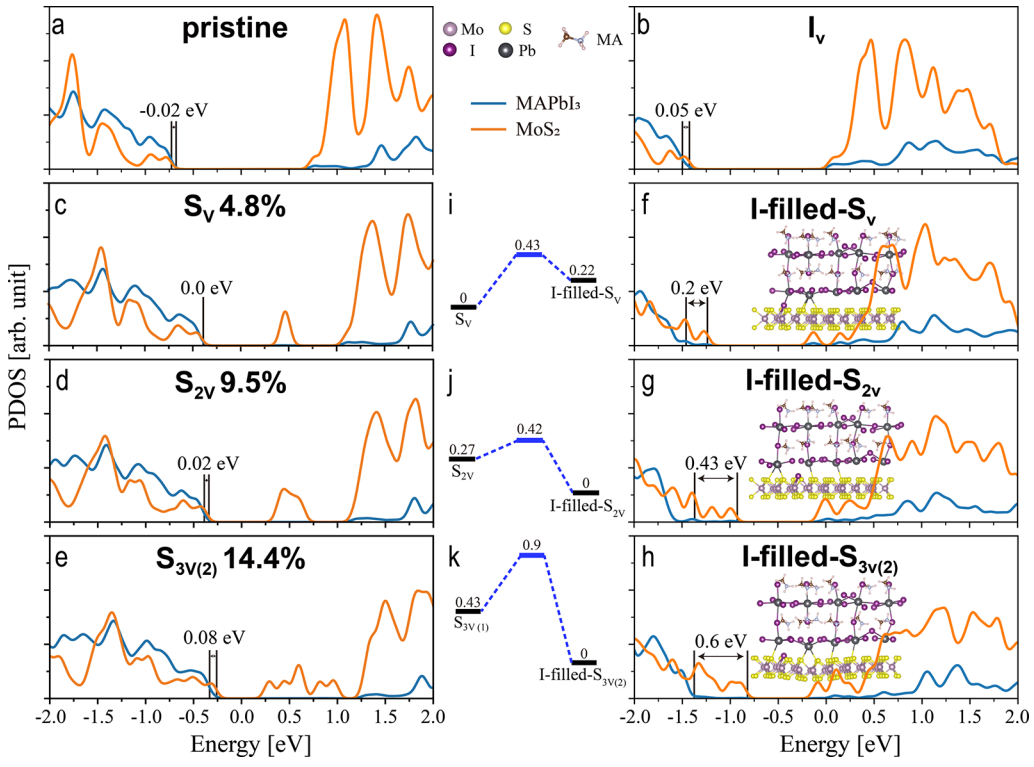

Figure 2. Projected density of states (PDOS) of the interface model shown in Figure 1 for (a) pristine, (b) I_V, (c and d) S_{nV} (n = 1−2), (e) $S_{3V(2)}$, and (f−h) corresponding I-filled configurations. Band offsets between $MAPbI_3$ and S_{nV}(n = 1−2), $S_{nV(2)}$ are weakly dependent on S_V concentration with band-offset changes less than ∼0.1 eV. Optimized configurations for I-filled configurations are shown in the insets of panels f−h. (i−k) Energy profile of the S_V-to-I_V process.

https://dx.doi.org/10.1021/acsenergylett.0c00485
ACS Energy Lett. 2020, 5, 1346−1354

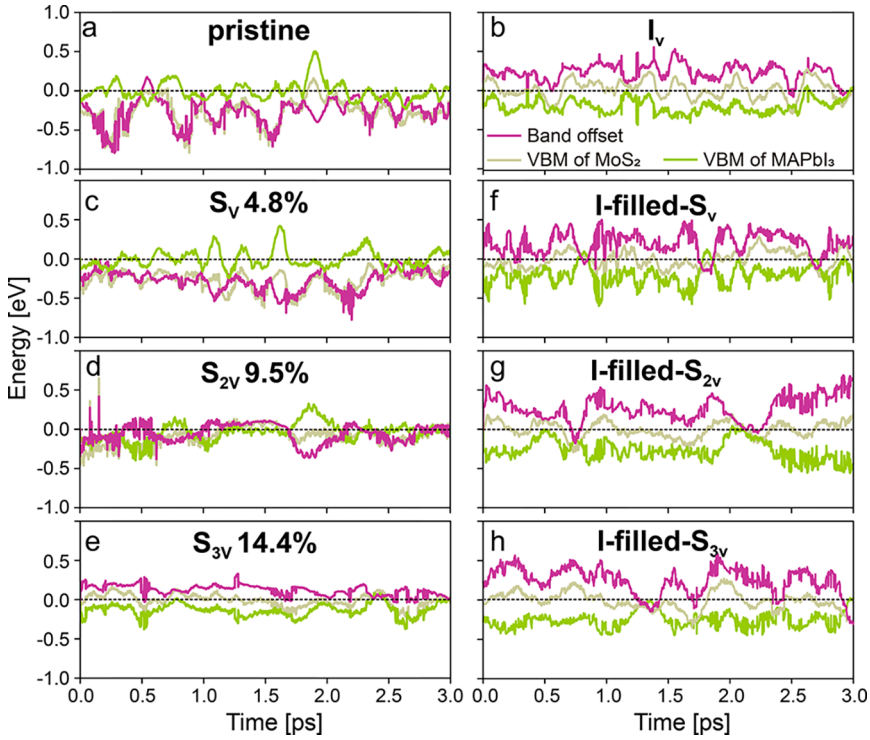

Figure 3. Time evolutions of the VBM band offset at 300 K. The positive band offsets indicate the VBM of MoS_2 is above that of $MAPbI_3$ which facilitates hole transport from $MAPbI_3$ to MoS_2.

respectively. Also, the total energy of I-filled-$S_{3V(1)}$ is lowered by 1.04 eV compared to the I-filled-$S_{3V(2)}$, although the $S_{3V(1)}$ configuration is higher in energy compared to $S_{3V(2)}$ for the isolated MoS_2 monolayer. Nudged elastic band (NEB)[72] calculations show relatively small iodine diffusion barriers of ~0.4, 0.1, and 0.5 eV for I-filled-S_{nV} (n = 1−2) and I-filled-$S_{nV(2)}$ respectively. Moreover, there is no barrier for $S_{3V(1)}$. That is, I-filled-$S_{3V(1)}$ spontaneously forms from $S_{3V(1)}$ after optimization. The small or no barriers explain why these structures are observed in the AIMD trajectory. Interestingly, we find that I-filled configurations have favorable band offset for hole transport from $MAPbI_3$ to MoS_2 as they lift the VBM of MoS_2 above $MAPbI_3$ by 0.2−0.6 eV (see Figures 2c−h and S5c). Therefore, this strongly suggests that the hole transport in $MAPbI_3/MoS_2$ is due to the S_V-to-I_V process.

Our conclusions on the band offsets are obtained from the analysis of static T = 0 K configurations. By conducting AIMD at room temperature to account for dynamic structural deformations, Figure 3 shows the dynamic band offsets along the AIMD trajectory. For example, we find that the band offsets for pristine and S_V configurations are negative for more than 97% of the AIMD trajectory, indicating unfavorable conditions for hole transfer. Increasing the S_V concentration to ~10% resulted in negative band offsets for approximately half of the AIMD trajectory. Further increase in the concentration to ~14.4% yields a positive band offset ~0.2 eV for more than 98% of the AIMD trajectory. In contrast, for the I-filled-S_{nV} (n = 1−2) and I-filled-$S_{3V(2)}$ configurations, the time-averaged band offsets are positive ~0.3 eV for 99% of the AIMD trajectory. Thus, I_V generation plays a key role in hole transport. The dynamic band offset of the pure I_V system (Figure 3b) further confirms the effect of I_V on band offset. In this case, the average offset is ~0.2 eV, although the static band offset is only 0.05 eV (Figure 2b), and charge-transfer hinder time is reduced to ~7% compared to the pristine interface. We have also calculated the interface dipole moment to confirm the conclusion. As shown in Figure 4, the interface dipoles of

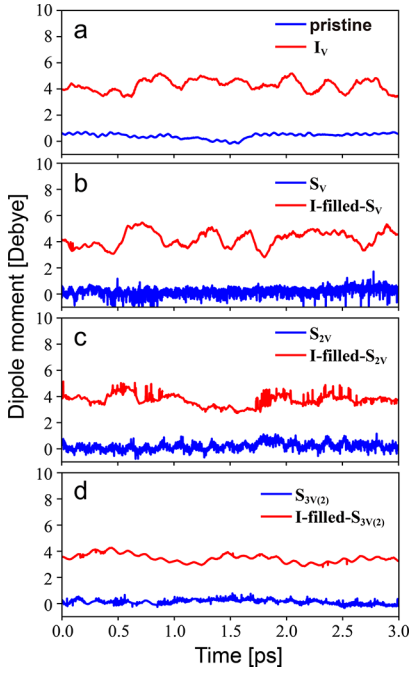

Figure 4. Time evolutions of the interface dipole moment at $MAPbI_3/MoS_2$ at 300 K calculated using $D_{interface} = D_{total} - D_{MAPbI_3}$. D_{total} is total dipole moment of $MAPbI_3/MoS_2$ heterostructure. D_{MAPbI_3} is the dipole moment of $MAPbI_3$ from frozen configuration of the interface. For I-filled configurations, the I atoms in S_V are not included into the $MAPbI_3$ slab.

https://dx.doi.org/10.1021/acsenergylett.0c00485
ACS Energy Lett. 2020, 5, 1346−1354

the pristine, S_{nV} (n = 1−2) and $S_{3V(2)}$ are close to zero. The I_V, I-filled-S_{nV} (n = 1−2), and I-filled-$S_{3V(2)}$ have a distinct interface dipole that successfully reverses the band offset.

Besides the band offset, we need further to investigate the charge-transfer dynamics at $MoS_2/MAPbI_3$ interface to confirm its HTM performance. The charge and the energy-transfer dynamics are fairly complicated because of two potential routes that the hole can take following its generation in the absorber material, as shown schematically in Figure 5.

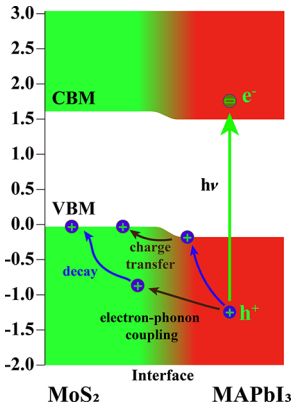

Figure 5. Schematic diagram of photoexcited hole dynamics at the $MAPbI_3/MoS_2$ interface. The charge-transfer and decay processes dominated by electron−phonon interaction are indicated by black and blue arrows, respectively.

First, the photoexcited hole can decay to the VBM of $MAPbI_3$ before hopping to the VBM of MoS_2. Second, the photoexcited hole can transfer to a deep MoS_2 level and then cool down to VBM of MoS_2. Previous studies reported long lifetime[73] and long nonequilibrium transport length[74] of hot carriers in MHPs, which suggests that the second route is highly likely. To account for all of these possibilities self-consistently, we have carried out *ab initio* NAMD simulations by employing fewest-switches surface-hopping (FSSH) technique (see Supplementary Note 3).[75] FSSH is the most popular surface-hopping scheme and has been tested extensively on realistic systems. This method is appropriate for studies of processes in which quantum transitions occur faster than quantum decoherence, such as intraband carrier relaxation and charge-transfer dynamics at interfaces.[76] However, decoherence effects must be taken into account when transition is slower than quantum decoherence, for instance, charge recombination in semiconductors.[52,77] Therefore, FSSH is appropriate for the current problem. Here we ignore electron−hole coupling as the exciton binding energy is low in MHP, and we focus only on hole transport.

We initiate the NAMD simulations by creating a hole in the absorber $MAPbI_3$ material ∼0.5 eV below the VBM. We follow the hole localization position along the NAMD trajectory by integrating the electron density over the region occupied by $MAPbI_3$ and MoS_2 (Supplementary Note 4). As shown in Figure 6, while the initial population of holes on $MAPbI_3$ exceeds 95%, it drops quickly to 55−65% within the first ∼20 fs because of hole transfer to MoS_2. This ultrafast process is mainly contributed by the adiabatic (AD) mechanism, which is induced by electron−phonon coupling that causes a crossing of KS states. The ∼20 fs ultrafast charge transfer is similar to what was observed before for MoS_2/WS_2 and MoS_2/C_{60} interfaces and is triggered by the A_{1g} optical phonon of MoS_2.[59,78]

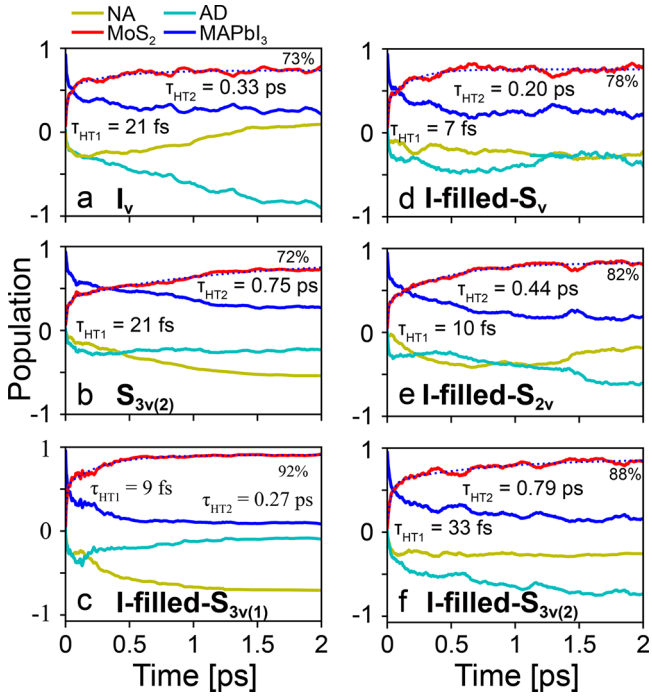

Figure 6. Time evolutions of hole population in $MAPbI_3/MoS_2$ interface with (a) I_V, (b) $S_{3v(2)}$, (c) I-filled-$S_{3V(1)}$, (d and e) I-filled-S_{nV} (n = 1−2), and (f) I-filled-$S_{3V(2)}$ during NAMD simulations. The nonadiabatic (NA) and adiabatic (AD) contributions to the charge transfer are shown in the lower part of each panel.

Following the ultrafast process, charge transfer continues but at a much slower time scale within 0.2−0.8 ps for the different systems. This process is due to both AD and NA mechanisms. The NA charge transfer is caused by charge hopping between different states. As seen from Figure 6, the slow hole-transfer process for I-filled-$S_{3V(2)}$ is faster than the corresponding one for $S_{3V(2)}$ by a factor of 3, which shows that the interplay of I_V and S_V accelerates charge-transfer time.

The asymptotic value of hole population on MoS_2 is less than one indicating that fraction of the hole density remains in $MAPbI_3$. This could be indicative of a finite probability for the hole to reflect to $MAPbI_3$. However, the hole will ultimately fully decay to VBM, and thus, the final hole population depends on the orbital hybridizations with the VBM. As seen from Figure 6, the final hole population on MoS_2 is ∼73%, ∼72%, and ∼92% for I_V, $S_{3V(2)}$, and I-filled-$S_{3V(1)}$ cases; 78% and 82% for I-filled-S_{nV} (n = 1−2); and 88% for I-filled-$S_{nV(2)}$. The increase of the transfer efficiency with vacancy concentration for the I-filled systems is in line with similar trends reported in the recent experimental results.[28] Further, the charge-transfer efficiency in I-filled configurations even with n = 1 is higher than that of I_V and S_{3V}, which demonstrates that the interplay of I_V and S_V also improves the charge-transfer efficiency. The hole energy decay dynamics is also analyzed and confirms this picture (Figures S7 and S8 and Supplementary Note 5).

We notice that experimentally the hole-transfer efficiency shows a linear trend with Sv concentration. Although the Sv concentration was not measured experimentally, the reported values in other studies range from 0.04%−4.4%. Here we show that the I-filled-S_V with 4.4% concentration has a charge-transfer efficiency of 78%, which is very close to the experimental value reported as 83%. However, it is challenging

https://dx.doi.org/10.1021/acsenergylett.0c00485
ACS Energy Lett. 2020, 5, 1346−1354

to investigate low concentrations of S_V to test the linear change trend because such simulations need much larger supercells and thus are unrealistic using the computationally expensive *ab initio* NAMD simulations.

Iodine brings in an extra electron when it occupies S_V site that can introduce a defect state and hence may act as a recombination center that could decrease the hole-transfer efficiency. To investigate this, we carry out a 3 ns NAMD simulation of hole recombination through the defect state in the bandgap. The results are shown in Figure S9. As seen from the figure, the nanosecond time scale of defect-induced recombination is about 3 orders of magnitude slower than the charge-transfer process. Thus, defect states introduced in I-filled systems are unlikely to hinder the charge-transfer process.

To reveal the probable hole-transfer through electron injection mechanism[34] from n-type bandgap states, we investigate the hole-transfer process from the VBM of $MAPbI_3$ to the bandgap states in MoS_2 by NAMD. This shows that the hole-transfer time through bandgap state is at the magnitude of nanosecond because of the large energy difference of VBM of $MAPbI_3$ and bandgap states at MoS_2. Such a time scale is longer than experiment results by 3 orders of magnitude, so the hole transfer at $MAPbI_3/MoS_2$ is unlikely through electron injection mechanism.

The mechanism of S_V-to-I_V to induce the interface dipole moment and reverse the band offset can be extended to other TMD systems as well as many ionic semiconductors. The p-type vacancies are generally positively charged, and iodine atoms can be attracted to fill these p-type vacancies. Then the I_V at the interface will induce the interface dipole moment and change the band offsets. Therefore, we propose that through the interplay between the vacancies at the interface, many TMDs and ionic semiconductors may improve their HTM performance. To support this claim, we test WS_2. The results are shown in Figure S10. For the pristine $MAPbI_3/WS_2$ heterostructure, the band offset of VBM is zero. For the I-filled-S_V case, the I_V-to-S_V process successfully increases the band offset to 0.21 eV, therefore facilitating ultrafast hole extraction.

We demonstrated a new mechanism to improve the HTM performance of TMDs based on the study of $MAPbI_3/MoS_2$. A cooperative effect between I_V in $MAPbI_3$ and S_V in MoS_2 plays a crucial role in reversing the band offset and accelerating hole transfer at the $MAPbI_3/MoS_2$ interface. S_V on their own cannot explain the enhancement of hole transport across the $MAPbI_3/MoS_2$ interface except if the doping concentration is larger than 20%. However, S_V even with a low concentration, can promote the formation of I_V at the interface, and the interface dipole induced by I_V reverses the band offset between MoS_2 and $MAPbI_3$, enhancing charge transport. We determined the charge-transfer time scale at the interface to be 0.2−0.8 ps, which is in line with the recent experimental results reported as 0.3−0.7 ps. Further, by comparing I-filled systems with I_V and S_{3V}, we demonstrated that the interplay between iodine and S_V not only improves the charge-transfer efficiency but also decreases the time-scale of charge transfer. Finally, we showed that I-filled defects introduce slow recombination centers that are not expected to hinder the charge-transfer process. We propose that the conclusion may be extended into other TMD systems as well as ionic semiconductors, yet more careful investigations in the future are necessary. Our results provide valuable insights into the optimization of carrier pathways to electrode in hybrid perovskite-based solar cells.

■ ASSOCIATED CONTENT

Supporting Information

The Supporting Information is available free of charge at https://pubs.acs.org/doi/10.1021/acsenergylett.0c00485.

Spin−orbit coupling and self-interaction error, interface models, *ab initio* nonadiabatic molecular dynamics (NAMD) method, charge-transfer dynamics, hole energy relaxation and transfer, Supplementary Notes 1−5, Figures S1−S10, and Tables S1−S4 (PDF)

■ AUTHOR INFORMATION

Corresponding Authors

Jin Zhao − *ICQD/Hefei National Laboratory for Physical Sciences at the Microscale, and CAS Key Laboratory of Strongly-Coupled Quantum Matter Physics, and Department of Physics and Synergetic Innovation Center of Quantum Information & Quantum Physics, University of Science and Technology of China, Hefei, Anhui 230026, China; Department of Physics and Astronomy, University of Pittsburgh, Pittsburgh, Pennsylvania 15260, United States;* orcid.org/0000-0003-1346-5280; Email: zhaojin@ustc.edu.cn

Wissam A. Saidi − *Department of Mechanical Engineering and Materials Science, University of Pittsburgh, Pittsburgh, Pennsylvania 15261, United States;* orcid.org/0000-0001-6714-4832; Email: alsaidi@pitt.edu

Authors

Yongliang Shi − *ICQD/Hefei National Laboratory for Physical Sciences at the Microscale, and CAS Key Laboratory of Strongly-Coupled Quantum Matter Physics, and Department of Physics, University of Science and Technology of China, Hefei, Anhui 230026, China; Center for Spintronics and Quantum Systems, State Key Laboratory for Mechanical Behavior of Materials, School of Materials Science and Engineering, Xi'an Jiaotong University, Xi'an, Shaanxi 710049, China;* orcid.org/0000-0002-1407-8031

Oleg V. Prezhdo − *Departments of Chemistry and Physics and Astronomy, University of Southern California, Los Angeles, California 90089, United States;* orcid.org/0000-0002-5140-7500

Complete contact information is available at: https://pubs.acs.org/10.1021/acsenergylett.0c00485

Notes

The authors declare no competing financial interest.

■ ACKNOWLEDGMENTS

W.A.S. acknowledges the financial support from the National Science Foundation (Award No. DMR-1809085). Y.S. acknowledges the support of National Natural Science Foundation of China (NSFC), Grant No. 11904353. J.Z. acknowledges the support of National Key Foundation of China, Department of Science and Technology, Grant Nos. 2017YFA0204904 and 2016YFA0200604; NSFC, Grant Nos. 11974322 and 11620101003. O.V.P. acknowledges funding from the U.S. National Science Foundation, Grant No. CHE-1900510. Calculations were performed in part at the Environmental Molecular Sciences Laboratory at the PNNL, a user facility sponsored by the DOE Office of Biological and Environmental Research, Argonne Leadership Computing Facility, which is a DOE Office of Science User Facility

https://dx.doi.org/10.1021/acsenergylett.0c00485
ACS Energy Lett. 2020, 5, 1346−1354

supported under Contract DE-AC02-06CH11357, and the Supercomputing Center at USTC.

REFERENCES

(1) Green, M. A.; Ho-Baillie, A. Perovskite Solar Cells: The Birth of a New Era in Photovoltaics. *ACS Energy Lett.* **2017**, *2*, 822−830.

(2) Kamat, P. V.; Bisquert, J.; Buriak, J. Lead-Free Perovskite Solar Cells. *ACS Energy Lett.* **2017**, *2*, 904−905.

(3) Meggiolaro, D.; De Angelis, F. First-Principles Modeling of Defects in Lead Halide Perovskites: Best Practices and Open Issues. *ACS Energy Lett.* **2018**, *3*, 2206−2222.

(4) National Renewable Energy Laboratory. Best Research-Cell Efficiencies Chart. https://www.nrel.gov/pv/assets/pdfs/best-research-cell-efficiencies.20190802.pdf.

(5) Green, M. A.; Ho-Baillie, A.; Snaith, H. J. The Emergence of Perovskite Solar Cells. *Nat. Photonics* **2014**, *8*, 506−514.

(6) Miyata, A.; Mitioglu, A.; Plochocka, P.; Portugall, O.; Wang, J. T.-W.; Stranks, S. D.; Snaith, H. J.; Nicholas, R. J. Direct Measurement of the Exciton Binding Energy and Effective Masses for Charge Carriers in Organic−Inorganic Tri-Halide Perovskites. *Nat. Phys.* **2015**, *11*, 582.

(7) Xing, G.; Mathews, N.; Sun, S.; Lim, S. S.; Lam, Y. M.; Gratzel, M.; Mhaisalkar, S.; Sum, T. C. Long-Range Balanced Electron-and Hole-Transport Lengths in Organic-Inorganic $Ch_3nh_3pbi_3$. *Science* **2013**, *342*, 344−347.

(8) Stranks, S. D.; Eperon, G. E.; Grancini, G.; Menelaou, C.; Alcocer, M. J. P.; Leijtens, T.; Herz, L. M.; Petrozza, A.; Snaith, H. J. Electron-Hole Diffusion Lengths Exceeding 1 Micrometer in an Organometal Trihalide Perovskite Absorber. *Science* **2013**, *342*, 341−344.

(9) Stavrakas, C.; Delport, G.; Zhumekenov, A. A.; Anaya, M.; Chahbazian, R.; Bakr, O. M.; Barnard, E. S.; Stranks, S. D. Visualizing Buried Local Carrier Diffusion in Halide Perovskite Crystals Via Two-Photon Microscopy. *ACS Energy Lett.* **2020**, *5*, 117−123.

(10) Ambrosio, F.; Meggiolaro, D.; Mosconi, E.; De Angelis, F. Charge Localization, Stabilization, and Hopping in Lead Halide Perovskites: Competition between Polaron Stabilization and Cation Disorder. *ACS Energy Lett.* **2019**, *4*, 2013−2020.

(11) Du, M. H. Efficient Carrier Transport in Halide Perovskites: Theoretical Perspectives. *J. Mater. Chem. A* **2014**, *2*, 9091−9098.

(12) Kim, J.; Lee, S.-H.; Lee, J. H.; Hong, K.-H. The Role of Intrinsic Defects in Methylammonium Lead Iodide Perovskite. *J. Phys. Chem. Lett.* **2014**, *5*, 1312−1317.

(13) Shan, W.; Saidi, W. A. Segregation of Native Defects to the Grain Boundaries in Methylammonium Lead Iodide Perovskite. *J. Phys. Chem. Lett.* **2017**, *8*, 5935−5942.

(14) Samu, G. F.; Scheidt, R. A.; Balog, A.; Janaky, C.; Kamat, P. V. Tuning the Excited-State Dynamics of Cul Films with Electrochemical Bias. *ACS Energy Lett.* **2019**, *4*, 702−708.

(15) Tan, H.; Jain, A.; Voznyy, O.; Lan, X.; Garcia de Arquer, F. P.; Fan, J. Z.; Quintero-Bermudez, R.; Yuan, M.; Zhang, B.; Sargent, E. H.; et al. Efficient and Stable Solution-Processed Planar Perovskite Solar Cells Via Contact Passivation. *Science* **2017**, *355*, 722−726.

(16) Andriambelaza, N. F.; Mapasha, R. E.; Chetty, N. First-Principles Studies of Chromium Line-Ordered Alloys in a Molybdenum Disulfide Monolayer. *J. Phys.: Condens. Matter* **2017**, *29*, 325504.

(17) Liu, J.; Wu, Y.; Qin, C.; Yang, X.; Yasuda, T.; Islam, A.; Zhang, K.; Peng, W.; Chen, W.; Han, L. A Dopant-Free Hole-Transporting Material for Efficient and Stable Perovskite Solar Cells. *Energy Environ. Sci.* **2014**, *7*, 2963−2967.

(18) Domanski, K.; Correa-Baena, J.-P.; Mine, N.; Nazeeruddin, M. K.; Abate, A.; Saliba, M.; Tress, W.; Hagfeldt, A.; Gratzel, M. Not All That Glitters Is Gold: Metal-Migration-Induced Degradation in Perovskite Solar Cells. *ACS Nano* **2016**, *10*, 6306−6314.

(19) Urieta-Mora, J.; Garcia-Benito, I.; Molina-Ontoria, A.; Martin, N. Hole Transporting Materials for Perovskite Solar Cells: A Chemical Approach. *Chem. Soc. Rev.* **2018**, *47*, 8541−8571.

(20) Singh, R.; Singh, P. K.; Bhattacharya, B.; Rhee, H.-W. Review of Current Progress in Inorganic Hole-Transport Materials for Perovskite Solar Cells. *Appl. Mater. Today* **2019**, *14*, 175−200.

(21) Saliba, M.; Correa-Baena, J.-P.; Wolff, C. M.; Stolterfoht, M.; Phung, N.; Albrecht, S.; Neher, D.; Abate, A. How to Make over 20% Efficient Perovskite Solar Cells in Regular (N-I-P) and Inverted (P-I-N) Architectures. *Chem. Mater.* **2018**, *30*, 4193−4201.

(22) Kroemer, H. Nobel Lecture: Quasielectric Fields and Band Offsets: Teaching Electrons New Tricks. *Rev. Mod. Phys.* **2001**, *73*, 783−793.

(23) Sherkar, T. S.; Momblona, C.; Gil-Escrig, L.; Bolink, H. J.; Koster, L. J. A. Jan Anton; Improving Perovskite Solar Cells: Insights from a Validated Device Model. *Adv. Energy Mater.* **2017**, *7*, 1602432.

(24) Pockett, A.; Carnie, M. J. Ionic Influences on Recombination in Perovskite Solar Cells. *ACS Energy Lett.* **2017**, *2*, 1683−1689.

(25) Wang, J.; Fu, W.; Jariwala, S.; Sinha, I.; Jen, A. K.-Y.; Ginger, D. S. Reducing Surface Recombination Velocities at the Electrical Contacts Will Improve Perovskite Photovoltaics. *ACS Energy Lett.* **2019**, *4*, 222−227.

(26) Yu, Z.; Sun, L. Recent Progress on Hole-Transporting Materials for Emerging Organometal Halide Perovskite Solar Cells. *Adv. Energy Mater.* **2015**, *5*, 1500213.

(27) Schulz, P. Interface Design for Metal Halide Perovskite Solar Cells. *ACS Energy Lett.* **2018**, *3*, 1287−1293.

(28) Peng, B.; Yu, G.; Zhao, Y.; Xu, Q.; Xing, G.; Liu, X.; Fu, D.; Liu, B.; Tan, J. R. S.; Tang, W.; Lu, H.; et al. Achieving Ultrafast Hole Transfer at the Monolayer MoS_2 and $CH_3NH_3PbI_3$ Perovskite Interface by Defect Engineering. *ACS Nano* **2016**, *10*, 6383−6391.

(29) Sim, D. M.; Kim, M.; Yim, S.; Choi, M.-J.; Choi, J.; Yoo, S.; Jung, Y. S. Controlled Doping of Vacancy-Containing Few-Layer MoS_2 Via Highly Stable Thiol-Based Molecular Chemisorption. *ACS Nano* **2015**, *9*, 12115−12123.

(30) Neal, A. T.; Pachter, R.; Mou, S. P-Type Conduction in Two-Dimensional MoS_2 Via Oxygen Incorporation. *Appl. Phys. Lett.* **2017**, *110*, 193103.

(31) Lee, S. Y.; Kim, U. J.; Chung, J.; Nam, H.; Jeong, H. Y.; Han, G. H.; Kim, H.; Oh, H. M.; Lee, H.; Kim, H.; et al. Large Work Function Modulation of Monolayer MoS_2 by Ambient Gases. *ACS Nano* **2016**, *10*, 6100−6107.

(32) Xing, W.; Chen, Y.; Wang, X.; Lv, L.; Ouyang, X.; Ge, Z.; Huang, H. Mos2 Quantum Dots with a Tunable Work Function for High-Performance Organic Solar Cells. *ACS Appl. Mater. Interfaces* **2016**, *8*, 26916−26923.

(33) Huang, P.; Wang, Z.; Liu, Y.; Zhang, K.; Yuan, L.; Zhou, Y.; Song, B.; Li, Y. Water-Soluble 2d Transition Metal Dichalcogenides as the Hole-Transport Layer for Highly Efficient and Stable P-I-N Perovskite Solar Cells. *ACS Appl. Mater. Interfaces* **2017**, *9*, 25323−25331.

(34) Najafi, L.; Taheri, B.; Martin-Garcia, B.; Bellani, S.; Di Girolamo, D.; Agresti, A.; Oropesa-Nunez, R.; Pescetelli, S.; Vesce, L.; Calabro, E.; et al. MoS_2 Quantum Dot/Graphene Hybrids for Advanced Interface Engineering of a Ch3nh3pbi3 Perovskite Solar Cell with an Efficiency of over 20%. *ACS Nano* **2018**, *12*, 10736−10754.

(35) Kim, Y. G.; Kwon, K. C.; Le, Q. V.; Hong, K.; Jang, H. W.; Kim, S. Y. Atomically Thin Two-Dimensional Materials as Hole Extraction Layers in Organolead Halide Perovskite Photovoltaic Cells. *J. Power Sources* **2016**, *319*, 1−8.

(36) Capasso, A.; Matteocci, F.; Najafi, L.; Prato, M.; Buha, J.; Cina, L.; Pellegrini, V.; Carlo, A. D.; Bonaccorso, F. Few-Layer MoS_2 Flakes as Active Buffer Layer for Stable Perovskite Solar Cells. *Adv. Energy Mater.* **2016**, *6*, 1600920.

(37) Huang, P.; Wang, Z.; Liu, Y.; Zhang, K.; Yuan, L.; Zhou, Y.; Song, B.; Li, Y. Water-Soluble 2d Transition Metal Dichalcogenides as the Hole-Transport Layer for Highly Efficient and Stable P−I−N Perovskite Solar Cells. *ACS Appl. Mater. Interfaces* **2017**, *9*, 25323−25331.

https://dx.doi.org/10.1021/acsenergylett.0c00485
ACS Energy Lett. 2020, 5, 1346−1354

(38) McDonnell, S.; Addou, R.; Buie, C.; Wallace, R. M.; Hinkle, C. L. Defect-Dominated Doping and Contact Resistance in MoS_2. *ACS Nano* **2014**, *8*, 2880−2888.
(39) Hong, J.; Hu, Z.; Probert, M.; Li, K.; Lv, D.; Yang, X.; Gu, L.; Mao, N.; Feng, Q.; Xie, L.; et al. Exploring Atomic Defects in Molybdenum Disulphide Monolayers. *Nat. Commun.* **2015**, *6*, 6293.
(40) Zhou, W.; Zou, X.; Najmaei, S.; Liu, Z.; Shi, Y.; Kong, J.; Lou, J.; Ajayan, P. M.; Yakobson, B. I.; Idrobo, J.-C. Intrinsic Structural Defects in Monolayer Molybdenum Disulfide. *Nano Lett.* **2013**, *13*, 2615−2622.
(41) Lu, C.-P.; Li, G.; Mao, J.; Wang, L.-M.; Andrei, E. Y. Bandgap, Mid-Gap States, and Gating Effects in Mos2. *Nano Lett.* **2014**, *14*, 4628−4633.
(42) Jeong, H. Y.; Lee, S. Y.; Ly, T. H.; Han, G. H.; Kim, H.; Nam, H.; Jiong, Z.; Shin, B. G.; Yun, S. J.; Kim, J.; et al. Visualizing Point Defects in Transition-Metal Dichalcogenides Using Optical Microscopy. *ACS Nano* **2016**, *10*, 770−777.
(43) Vancso, P.; Magda, G. Z.; Peto, J.; Noh, J.-Y.; Kim, Y.-S.; Hwang, C.; Biro, L. P.; Tapaszto, L. The Intrinsic Defect Structure of Exfoliated Mos2 Single Layers Revealed by Scanning Tunneling Microscopy. *Sci. Rep.* **2016**, *6*, 29726.
(44) Elmelund, T.; Seger, B.; Kuno, M.; Kamat, P. V. How Interplay between Photo and Thermal Activation Dictates Halide Ion Segregation in Mixed Halide Perovskites. *ACS Energy Lett.* **2020**, *5*, 56−63.
(45) Kresse, G.; Hafner, J. Ab Initio Molecular Dynamics for Liquid Metals. *Phys. Rev. B: Condens. Matter Mater. Phys.* **1993**, *47*, 558−561.
(46) Kresse, G.; Hafner, J. Ab Initio Molecular Dynamics for Open-Shell Transition Metals. *Phys. Rev. B: Condens. Matter Mater. Phys.* **1993**, *48*, 13115−13118.
(47) Kresse, G.; Hafner, J. Ab-Initio Molecular-Dynamics Simulation of the Liquid-Metal Amorphous-Semiconductor Transition in Germanium. *Phys. Rev. B: Condens. Matter Mater. Phys.* **1994**, *49*, 14251−14269.
(48) Nie, X.-R.; Sun, B.-Q.; Zhu, H.; Zhang, M.; Zhao, D.-H.; Chen, L.; Sun, Q.-Q.; Zhang, D. W. Impact of Metal Contacts on the Performance of Multilayer Hfs2 Field-Effect Transistors. *ACS Appl. Mater. Interfaces* **2017**, *9*, 26996−27003.
(49) Akimov, A. V.; Prezhdo, O. V. The Pyxaid Program for Non-Adiabatic Molecular Dynamics in Condensed Matter Systems. *J. Chem. Theory Comput.* **2013**, *9*, 4959−4972.
(50) Chu, W.; Saidi, W. A.; Zheng, Q.; Xie, Y.; Lan, Z.; Prezhdo, O. V.; Petek, H.; Zhao, J. Ultrafast Dynamics of Photongenerated Holes at a CH_3OH/TiO_2 Rutile Interface. *J. Am. Chem. Soc.* **2016**, *138*, 13740−13749.
(51) He, J.; Fang, W.-H.; Long, R.; Prezhdo, O. V. Increased Lattice Stiffness Suppresses Nonradiative Charge Recombination in $MAPbI_3$ Doped with Larger Cations: Time Domain Ab Initio Analysis. *ACS Energy Lett.* **2018**, *3*, 2070−2076.
(52) Zhang, L.; Zheng, Q.; Xie, Y.; Lan, Z.; Prezhdo, O. V.; Saidi, W. A.; Zhao, J. Delocalized Impurity Phonon Induced Electron-Hole Recombination in Doped Semiconductors. *Nano Lett.* **2018**, *18*, 1592−1599.
(53) Li, W.; Tang, J.; Casanova, D.; Prezhdo, O. V. Time-Domain Ab Lnitio Analysis Rationalizes the Unusual Temperature Dependence of Charge Carrier Relaxation in Lead Halide Perovskite. *ACS Energy Lett.* **2018**, *3*, 2713−2720.
(54) Tong, C.-J.; Geng, W.; Prezhdo, O. V.; Liu, L.-M. Role of Methylammonium Orientation in Ion Diffusion and Current Voltage Hysteresis in the $CH_3NH_3PbI_3$ Perovskite. *ACS Energy Lett.* **2017**, *2*, 1997−2004.
(55) Long, R.; Fang, W.; Prezhdo, O. V. Moderate Humidity Delays Electron-Hole Recombination in Hybrid Organic-Inorganic Perovskites: Time-Domain Ab Initio Simulations Rationalize Experiments. *J. Phys. Chem. Lett.* **2016**, *7*, 3215−3222.
(56) Long, R.; Prezhdo, O. V. Dopants Control Electron-Hole Recombination at Perovskite-Tio2 Interfaces: Ab Initio Time-Domain Study. *ACS Nano* **2015**, *9*, 11143−11155.
(57) Li, W.; Liu, J.; Bai, F.-Q.; Zhang, H.-X.; Prezhdo, O. V. Hole Trapping by Iodine Interstitial Defects Decreases Free Carrier Losses in Perovskite Solar Cells: A Time-Domain Ab Initio Study. *ACS Energy Lett.* **2017**, *2*, 1270−1278.
(58) Wang, L.; Long, R.; Prezhdo, O. V. Time-Domain Ab Initio Modeling of Photoinduced Dynamics at Nanoscale Interfaces. *Annu. Rev. Phys. Chem.* **2015**, *66*, 549−579.
(59) Zheng, Q.; Saidi, W. A.; Xie, Y.; Lan, Z.; Prezhdo, O. V.; Petek, H.; Zhao, J. Jin; Phonon-Assisted Ultrafast Charge Transfer at Van Der Waals Heterostructure Interface. *Nano Lett.* **2017**, *17*, 6435−6442.
(60) Nie, Z.; Shi, Y.; Qin, S.; Wang, Y.; Jiang, H.; Zheng, Q.; Cui, Y.; Meng, Y.; Song, F.; Wang, X.; et al. Tailoring Exciton Dynamics of Monolayer Transition Metal Dichalcogenides by Interfacial Electron-Phonon Coupling. *Commun. Phys.* **2019**, *2*, 103.
(61) Kresse, G.; Joubert, D. From Ultrasoft Pseudopotentials to the Projector Augmented-Wave Method. *Phys. Rev. B: Condens. Matter Mater. Phys.* **1999**, *59*, 1758−1775.
(62) Kresse, G.; Hafner, J. Ab Initio Molecular Dynamics for Liquid Metals. *Phys. Rev. B: Condens. Matter Mater. Phys.* **1993**, *47*, 558−561.
(63) Mak, K. F.; Lee, C.; Hone, J.; Shan, J.; Heinz, T. F. Atomically Thin Mos_2: A New Direct-Gap Semiconductor. *Phys. Rev. Lett.* **2010**, *105*, 136805.
(64) Hu, C.; Yuan, C.; Hong, A.; Guo, M.; Yu, T.; Luo, X. Xingfang; Work Function Variation of Monolayer Mos_2 by Nitrogen-Doping. *Appl. Phys. Lett.* **2018**, *113*, 041602.
(65) Gong, C.; Zhang, H.; Wang, W.; Colombo, L.; Wallace, R. M.; Cho, K. Band Alignment of Two-Dimensional Transition Metal Dichalcogenides: Application in Tunnel Field Effect Transistors. *Appl. Phys. Lett.* **2013**, *103*, 053513.
(66) Madjet, M. E.; El-Mellouhi, F.; Carignano, M. A.; Berdiyorov, G. R. Atomic Partial Charges on $CH_3NH_3PbI_3$ from First-Principles Electronic Structure Calculations. *J. Appl. Phys.* **2016**, *119*, 165501.
(67) Zhang, X.; Shen, J.-X.; Wang, W.; Van de Walle, C. G. First-Principles Analysis of Radiative Recombination in Lead-Halide Perovskites. *ACS Energy Lett.* **2018**, *3*, 2329−2334.
(68) Choe, D.-H.; West, D.; Zhang, S. Band Alignment and the Built-in Potential of Solids. *Phys. Rev. Lett.* **2018**, *121*, 196802.
(69) Saidi, W. A.; Ponce, S.; Monserrat, B. Temperature Dependence of the Energy Levels of Methylammonium Lead Iodide Perovskite from First-Principles. *J. Phys. Chem. Lett.* **2016**, *7*, 5247−5252.
(70) Foley, B. J.; Marlowe, D. L.; Sun, K.; Saidi, W. A.; Scudiero, L.; Gupta, M. C.; Choi, J. J. Temperature Dependent Energy Levels of Methylammonium Lead Iodide Perovskite. *Appl. Phys. Lett.* **2015**, *106*, 243904.
(71) Saidi, W. A.; Kachmar, A. Effects of Electron−Phonon Coupling on Electronic Properties of Methylammonium Lead Iodide Perovskites. *J. Phys. Chem. Lett.* **2018**, *9*, 7090−7097.
(72) Henkelman, G.; Jonsson, H. Improved Tangent Estimate in the Nudged Elastic Band Method for Finding Minimum Energy Paths and Saddle Points. *J. Chem. Phys.* **2000**, *113*, 9978−9985.
(73) Zhu, H.; Miyata, K.; Fu, Y.; Wang, J.; Joshi, P. P.; Niesner, D.; Williams, K. W.; Jin, S.; Zhu, X.- Y. Screening in Crystalline Liquids Protects Energetic Carriers in Hybrid Perovskites. *Science* **2016**, *353*, 1409−1413.
(74) Guo, Z.; Wan, Y.; Yang, M.; Snaider, J.; Zhu, K.; Huang, L. Long-Range Hot-Carrier Transport in Hybrid Perovskites Visualized by Ultrafast Microscopy. *Science* **2017**, *356*, 59.
(75) Tully, J. C. Molecular Dynamics with Electronic Transitions. *J. Chem. Phys.* **1990**, *93*, 1061−1071.
(76) Long, R.; English, N. J.; Prezhdo, O. V. Photo-Induced Charge Separation across the Graphene-TiO_2 Interface Is Faster Than Energy Losses: A Time-Domain Ab Lnitio Analysis. *J. Am. Chem. Soc.* **2012**, *134*, 14238−14248.
(77) Jaeger, H. M.; Fischer, S.; Prezhdo, O. V. Decoherence-Induced Surface Hopping. *J. Chem. Phys.* **2012**, *137*, 22A545.

https://dx.doi.org/10.1021/acsenergylett.0c00485
ACS Energy Lett. 2020, 5, 1346−1354

(78) Guo, H.; Zhao, C.; Zheng, Q.; Lan, Z.; Prezhdo, O. V.; Saidi, W. A.; Zhao, J. Superatom Molecular Orbital as an Interfacial Charge Separation State. *J. Phys. Chem. Lett.* **2018**, *9*, 3485−3490.

https://dx.doi.org/10.1021/acsenergylett.0c00485
ACS Energy Lett. 2020, 5, 1346−1354